

ACCEPTED MANUSCRIPT

# Optimization design of lightweight structure inspired by glass sponges (Porifera, Hexacinellida) and its mechanical properties

To cite this article before publication: Longhai Li *et al* 2020 *Bioinspir. Biomim.* in press <https://doi.org/10.1088/1748-3190/ab6ca9>

## Manuscript version: Accepted Manuscript

Accepted Manuscript is “the version of the article accepted for publication including all changes made as a result of the peer review process, and which may also include the addition to the article by IOP Publishing of a header, an article ID, a cover sheet and/or an ‘Accepted Manuscript’ watermark, but excluding any other editing, typesetting or other changes made by IOP Publishing and/or its licensors”

This Accepted Manuscript is © 2019 IOP Publishing Ltd.

During the embargo period (the 12 month period from the publication of the Version of Record of this article), the Accepted Manuscript is fully protected by copyright and cannot be reused or reposted elsewhere.

As the Version of Record of this article is going to be / has been published on a subscription basis, this Accepted Manuscript is available for reuse under a CC BY-NC-ND 3.0 licence after the 12 month embargo period.

After the embargo period, everyone is permitted to use copy and redistribute this article for non-commercial purposes only, provided that they adhere to all the terms of the licence <https://creativecommons.org/licences/by-nc-nd/3.0>

Although reasonable endeavours have been taken to obtain all necessary permissions from third parties to include their copyrighted content within this article, their full citation and copyright line may not be present in this Accepted Manuscript version. Before using any content from this article, please refer to the Version of Record on IOPscience once published for full citation and copyright details, as permissions will likely be required. All third party content is fully copyright protected, unless specifically stated otherwise in the figure caption in the Version of Record.

View the [article online](#) for updates and enhancements.

1  
2  
3  
4  
5  
6  
7  
8  
9  
10  
11  
12  
13  
14  
15  
16  
17  
18  
19  
20  
21  
22  
23  
24  
25  
26  
27  
28  
29  
30  
31  
32  
33  
34  
35  
36  
37  
38  
39  
40  
41  
42  
43  
44  
45  
46  
47  
48  
49  
50  
51  
52  
53  
54  
55  
56  
57  
58  
59  
60

**Optimization design of lightweight structure inspired by glass  
sponges (Porifera, Hexacinellida) and its mechanical properties**

Longhai Li<sup>1,2</sup>, Ce Guo<sup>2,\*</sup>, Yiting Chen<sup>2,\*</sup>, Yinhe Chen<sup>2,3</sup>

*1 College of Mechanical and Electrical Engineering, Nanjing University of Aeronautics and  
Astronautics, 29 Yudao Street, Nanjing, 210016, People's Republic of China*

*2 Institute of Bio-inspired Structure and Surface Engineering, Nanjing University of Aeronautics  
and Astronautics, 29 Yudao Street, Nanjing, 210016, People's Republic of China*

*3 Shanghai Institute of Spaceflight Control Technology, Shanghai 201109, China*

\*Corresponding author: Prof. Ce Guo, E-mail address: [guozc@nuaa.edu.cn](mailto:guozc@nuaa.edu.cn). Tel.:  
+8613951759371.

**Abstract:** The glass sponge is a porous lightweight structure in the deep sea. It has high toughness, high strength, and high stability. In this work, a super-depth-of-field microscope was employed to observe the microstructure of the glass sponge. Based on its morphological characteristics, two novel bio-inspired lightweight structures were proposed, and the finite-element analyses (FEA) of the structures were carried out under compression, torsion, and bending loads, respectively. The structure samples were fabricated using stereolithography 3D-printing technology, and the dimension sizes of the samples were equal to those of the corresponding FEA models. Mechanical tests were performed on an electronic universal testing machine, and the results were used to demonstrate the reliability of the FEA. Additionally, lightweight numbers (LWN) were proposed to evaluate the lightweight efficiency, and a honeycomb structure was selected as the reference structure. The results indicate that the lightweight numbers of the novel bio-inspired structures are higher than those of the honeycomb structure, respectively. Finally, the proposed structures were optimized by the response surface, BP (Back Propagation) and GA-BP (Genetic Algorithm optimized Back Propagation) method. The results show that GA-BP model after training has a high accuracy. These results can provide significant guidance for the design of tube-shaped, thin-walled structures in the engineering.

**Keywords:** glass sponges; microstructure; mechanical properties; lightweight numbers; optimization; bio-inspired

1  
2  
3  
4  
5  
6  
7  
8  
9  
10  
11  
12  
13  
14  
15  
16  
17  
18  
19  
20  
21  
22  
23  
24  
25  
26  
27  
28  
29  
30  
31  
32  
33  
34  
35  
36  
37  
38  
39  
40  
41  
42  
43  
44  
45  
46  
47  
48  
49  
50  
51  
52  
53  
54  
55  
56  
57  
58  
59  
60

45     **1 Introduction**

46         To adapt to variable and complicated requirements, especially, in aerospace  
47     engineering, researchers need to design structures that have high lightweight numbers,  
48     while simultaneously maintaining the remarkable mechanical properties as high  
49     specific strength, specific stiffness, and damage resistance (Jiao et al, 2010; Guo et al,  
50     2012; Li et al, 2017). These lightweight structures not only reduce the storage  
51     consumption of raw materials and energy but also improve the performance of  
52     constructing and manufacturing systems. In this work, the selected case study is a  
53     load-bearing robot arm structures for aerospace applications. The elements between  
54     joints are generally tubular structures to permit wires to be internally channeled within  
55     the structure. However, some traditional thin-walled tube structures, such as normal  
56     circular-section tubes, cannot have their weight reduced effectively. In solving this  
57     problem, scientists and engineers are seeking new solutions.

58         Highly efficient natural structures have become optimized over millions of years,  
59     with a minimum of materials and energy but high strength and maximal stability,  
60     which engineers can use for reference and imitation. The structures of living  
61     organisms (such as animal bones, honeycombs, elytra, bamboo, rostra, and beaks)  
62     have evolved into having a low weight and excellent damage resistance abilities,  
63     which provide inexhaustible prototypes and ingenious templates for human technical  
64     improvements and innovations (Aizenberg & Hendler, 2004; Zhao et al, 2010; Zhao  
65     et al, 2010). For instance, inspired by the rotated plywood structure of bone tissue, a  
66     kind of biomimetic tissue scaffold was designed and manufactured to treat some bone

defects (Yu et al, 2017). Chen et al. studied the lightweight structure and mechanical properties of a luffa sponge, and, as a result, new biomimetic foams that can be applied in anticrushing devices and superlight sandwich panels were fabricated (Chen et al, 2014). Based on the investigation of the geometrical characteristics and structure of bamboo weevil larva, bionic lightweight blades were designed and manufactured. The experimental results showed that these blades can improve the working efficiency of a mincing machine (Tong et al, 2017). Researchers believed that the elytra must be lightweight with optimized structures and excellent mechanical properties, and this could inspire the structure, element, or part design in aircraft and spacecraft (Smith et al, 2000; Yang & Dai, 2010; Sun & Bhushan, 2012). Chen et al. found a new biomimetic structure in beetle elytra, and the structural characteristics, mechanical properties, and their strengthening mechanism of high energy absorption were investigated. The results show the potential for its application as a novel sandwich structure in the engineering field (Chen et al, 2017a; Chen et al, 2017b; Zhang et al, 2017). Another study found that the structure of bamboo can reduce self-weight effectively and increase the axial and lateral energy absorption of thin-walled tubes (Parameswaran & Liese, 1976; Li et al, 1995; Zou et al, 2016). The biomimetic structural models can solve certain engineering problems.

Glass sponges represent a successful evolution in nature, living on the bottom of the sea at depths from 10 to 6770 m (Drozdov & Karpenko, 2011; Leys et al, 2016; Dohrmann et al, 2017). The sponge is anchored to the sea floor by thousands of anchor spicules (long, hair-like skeletal elements), each of which measures 50  $\mu\text{m}$  in

1  
2  
3  
4  
5  
6  
7  
8  
9  
10  
11  
12  
13  
14  
15  
16  
17  
18  
19  
20  
21  
22  
23  
24  
25  
26  
27  
28  
29  
30  
31  
32  
33  
34  
35  
36  
37  
38  
39  
40  
41  
42  
43  
44  
45  
46  
47  
48  
49  
50  
51  
52  
53  
54  
55  
56  
57  
58  
59  
60

89 diameter and up to 100 mm in length. The wall thickness of the sponge is usually 1–2  
90 mm, while the longest can grow to ~2 m. Because of its special lattice formation, the  
91 sponges construct a porous skeleton structure with light weight, high toughness, high  
92 strength, and high stability. The structure can successfully avoid being broken and  
93 swept away by the ocean currents. However, many studies of glass sponges focused  
94 on their morphology, biological characteristics, structure properties, etc. (Aizenberg et  
95 al, 2004; Leys et al, 2007; Monn et al, 2015), while few studies inspired by  
96 lightweight structural design based on glass sponges for manufacturing and  
97 mechanical analysis have been reported.

98 Using nature as the archetype for exploring lightweight design solutions is an  
99 efficient way to gain innovative construction principles; thus, a suitable natural  
100 archetype is necessary (Maier et al, 2013). Glass sponges were chosen as the bionic  
101 object with the above observation in mind; two novel bio-inspired thin-walled  
102 tube-like lightweight structures were developed and their mechanical properties  
103 investigated. The results have high significance for the design of lightweight  
104 structures and have potential for thin-walled structures in a robot arm for aerospace  
105 engineering and other tubular structures.

106

107 **2 Materials and methods**

108 **2.1 Materials**

109 The sample of the glass sponges (Porifera, Hexacinellida) was collected from  
110 Hainan province, China. The optical microscope observation and mechanical

properties test (including compression, torsion and bending tests, etc) were performed at the Institute of Bio-inspired Structure and Surface Engineering, Nanjing University of Aeronautics and Astronautics. The body-lengths range from 30cm to 60cm. The tests were kept under a natural light cycle, at a temperature of  $(25 \pm 2) ^\circ\text{C}$  and a humidity of 50 %–80 %.

## 2.2 Mechanical properties test

### 2.2.1 Experiment setup

Due to the complicated morphology of bio-inspired structures, 3D printing technology was the most suitable method for sample manufacture. The mechanical properties of the glass sponge-inspired structures were investigated. Compression and bending test were conducted on universal testing machine (Instron-5566) and torsion test was performed by torsion testing machine (QBN100-L100). The load velocity of 2mm/min was set to carry out the compression tests and the force-displacement curves are obtained. For bending tests, the fixture of samples was specially designed and built. The experimental platform was shown in Fig. S1.

### 2.2.2 Lightweight numbers

Lightweight efficiency of the structure is usually measured by specific strength and it can be calculated as follows (Guo et al, 2012):

$$p = \frac{\sigma_b}{\rho} = \frac{\sigma_b V}{m} \quad (1)$$

Where  $p$  represents specific strength,  $\sigma_b$  represents fracture strength,  $\rho$  represents apparent density,  $V$  represents apparent volume which includes structural

entity and closed pore volume,  $m$  represents mass.

In this paper, due to the same apparent volume and cross-sectional area of each bio-inspired structure, the evaluation efficiency also can be determined by Lightweight Numbers (LWN) as follows (Bukner et al, 2015):

$$\text{LWN} = \frac{\text{Maxload}}{\text{Weight}} \quad (2)$$

LWN is an important coefficient to evaluate the lightweight efficiency of each model. The higher the LWN, the higher the lightweight efficiency of the structure is (Sven et al, 2015). Here, there are three kinds of LW-numbers:

LWN-C – Compression,

LWN-T – Torsion,

LWN-B – Bending.

### 2.3 Principle of BP neural network

BP neural network is a feed-forward neural network with an input layer, one or more hidden layers and an output layer in which all the neurons are connected, it is widely used in nonlinear fitting. The steps of the BP neural network are as follows (Wang et al, 2013):

Step 1: Data standardization

The input sample is defined as  $x = (x_1 \ x_2 \ \dots \ x_N)^T$ , and the corresponding expected output is  $y = (y_1 \ y_2 \ \dots \ y_h)^T$ . The raw data should be normalized according to the following equation.

$$x' = \frac{x_i - \min(x)}{\max(x) - \min(x)} \quad (3)$$



Where  $x$  represents raw data,  $x'$  represents dimensionless data.

Step 2: Calculation the output of each layer

Initialization function is assigned to the connection weight and threshold of each layer. The values of hidden and output layers are calculated by the Sigmoid function, and each node can be obtained as follows:

$$H_j = f\left(\sum_{i=1}^n w_{ij}x_i - a_j\right), j=1,2,\dots,l \quad (4)$$

$$O_k = \sum_{j=1}^l H_j w_{jk} - b_k, k=1,2,\dots,m \quad (5)$$

$$f(x) = \frac{1}{1+e^{-x}} \quad (6)$$

Where  $n$  and  $l$  are the numbers of the input and hidden layers, respectively;  $H_j$ ,  $O_k$  represent the output of hidden layer and output layer, respectively;  $w_{ij}$ ,  $w_{jk}$  represent the connection weight;  $a_j$ ,  $b_k$  represent the threshold of hidden and output layers, respectively; and  $f(x)$  represents activation functions.

Step 3: Error calculation

$e_k$  represents the mean square of the deviation between the network's expected output and predicted output, which can be obtained as follows:

$$e_k = Y_k - O_k \quad (7)$$

Where  $Y_k$  represents expected output.

Step 4: Update weight coefficient and threshold

The weight and threshold of each layer can be adjusted according to the error between expected output and predicted output, which can be expressed as follows:

$$w_{ij} = w_{ij} + \eta H_j (1 - H_j) x(i) \sum_{k=1}^m w_{jk} e_k, i = 1, 2, \dots, n; j = 1, 2, \dots, l \quad (8)$$

$$w_{jk} = w_{jk} + \eta H_j e_k, j = 1, 2, \dots, l; k = 1, 2, \dots, m \quad (9)$$

$$a_j = a_j + \eta H_j (1 - H_j) \sum_{k=1}^m w_{jk} e_k, j = 1, 2, \dots, l \quad (10)$$

$$b_k = b_k + \eta e_k, k = 1, 2, \dots, m \quad (11)$$

Where  $\eta$  is the learning rate.

Step 5: Judgement algorithm iteration

When the network is trained, the errors of the neurons in the output layer propagate back to the hidden and input layers, and the weights between the layers are constantly corrected. If the requirements are satisfied, the iteration calculation ends. Otherwise, step 2 is repeated until the system's mean square error is minimized and the topology structures of BP neural network are shown in Fig. S2.

## 2.4 GA Optimized BP algorithm

In order to overcome the defect of BP neural network that the gradient descent method makes the algorithm easily fall into local optimal value in the learning process, GA optimized BP algorithm was proposed. The specific steps of GA optimize BP are as follows (Wang et al, 2013):

Step 1: Encoding and initializing population

According to the topological structure of BP neural network in the actual assembly, the individual length  $S$  can be decided:

$$S = R * S_1 + S_1 * S_2 + S_1 + S_2 \quad (12)$$

Where  $R$ ,  $S_1$ ,  $S_2$  represent the nodes number of the input layer, hidden layer and output layer, respectively.

### Step 2: Fitness function

The absolute value of error between the predict output and expected value is defined as the value of fitness, it can be expressed as follows:

$$F = k \left( \sum_{i=1}^n (|y_i - o_i|) \right) \quad (13)$$

Where  $y_i$  represents the expected value of  $i$ th-node;  $o_i$  represents the predicted value of  $i$ th-node;  $n$  represents the total output nodes;  $k$  represents the scaling factor.

### Step 3: Selection operation

In this paper, roulette method was used to select some good individuals to the next generation group. The chosen probability of every individual  $p_i$  can be calculated as follows:

$$f_i = \frac{k}{F_i} \quad (14)$$

$$p_i = \frac{f_i}{\sum_{j=1}^N f_j} \quad (15)$$

Where  $F_i$  is the adaptive value of  $i$ ;  $k$  is coefficient;  $N$  is the number of the individuals.

### Step 4: Crossover operation

For each individual pair, with a certain probability (crossover probability), exchanging some parts of their gene. The chromosome  $a_p$  and  $a_t$  do crossover in  $q$  as follows:

$$a_{pq} = a_{pq}(1-b) + a_{tq}b \quad (16)$$

$$a_{tq} = a_{tq}(1-b) + a_{pq}b \quad (17)$$

Where  $b$  represents a random number between 0 and 1.

## Step 5: Mutation operation

Using non-uniform variation to change the probability of mutation, and the gene  $r$  of the individual  $s$  can be varied as follows:

$$a_{rs} = \begin{cases} a_{rs} + (a_{rs} - a_{\max}) * f(g) & h > 0.5 \\ a_{rs} + (a_{\min} - a_{rs}) * f(g) & h \leq 0.5 \end{cases} \quad (18)$$

Where  $a_{\max}$  is the upper bound of gene;  $a_{\min}$  is the lower bound;  $f(g) = r_2 * (1 - g/G_{\max})^2$ ;  $r_2$  is a random number;  $g$  is the iteration time;  $G_{\max}$  is the maximum evolutionary number;  $r$  is the random number between 0 and 1.

## Step 6: Termination condition judgment

Repeat steps 2 - 5 until reach the iteration goal or the number of iterations. The flowchart of GA optimize BP algorithm can be summarized as Fig. S3.

## 3 Results

### 3.1 Biological characteristics

#### 3.1.1 Microscope observation

The macrostructures and microstructures of the specimen were observed using a super-depth-of-field microscope. Figures 1(a) and (b) show that the skeleton of the porous glass sponge is cylindrical, and there are many small holes in the wall of the skeleton, called "wall holes," that are the main cause of structural weight reduction. Initial surveys of the skeletal lattice suggest that the sponge is principally composed of a series of overlapping vertical, horizontal, and diagonal fibrous struts, forming an underlying quadrate lattice that is principally composed of a network structure and octagon mesh, as in Figures 1(c) and (d). These structure characteristics are illustrated

in Figure 1(d).

Moreover, outside of the horizontal and vertical struts is an additional set of orthogonal struts, each consisting of similarly bundled spicules, oriented diagonally (at approximately  $45^\circ$  to the cylinder axis) and surrounding the tube in oblique spirals, which are called “wall ridges.” The spiral ridges outside the porous sponge wall also have a unique structure, with a thickness of 2–10 mm and a cross section showing a smaller triangle. The ridges spiral along the axis of the skeleton at  $\pm 45^\circ$ . Generally, the positive (or reverse) helix rises half a circle, suddenly turns  $90^\circ$ , and then the reverse (or positive) spiral rises in Figures 1(e) and (f).

**Figure 1.** Macrostructures and microstructures of the sample: (a) specimen, (b) a part of the specimen, (c) the macrostructures and microstructures, (d) details of the macrostructures and microstructures in an enlarged view (blue line represents the main skeleton including network structure and octagon mesh), (e) wall ridges, and (f) details of the wall ridges

Fig. S4 shows the inclined supporting struts numbered from 0 to 15, and the outer spiral ridges are shown in red. For the glass sponges, the two adjacent parallel supporting struts form one group (such as 1 and 2, 3 and 4, 5 and 6, and so on). If one group of spiral struts develops an outer spiral ridge, for example group (1, 2) and group (9,10), then the neighboring group of spiral ribs that are in the same direction will not grow an outer ridge, such as group (5, 6) and group (13, 14). According to this structural feature, the unfolded diagram is designed, as shown in Fig. S4.

### 3.1.2 Bio-inspired design of lightweight tubular structure

In this section, two novel bio-inspired tubular structures were proposed. Figure 2

1  
2  
3  
4  
5  
6  
7  
8  
9  
10  
11  
12  
13  
14  
15  
16  
17  
18  
19  
20  
21  
22  
23  
24  
25  
26  
27  
28  
29  
30  
31  
32  
33  
34  
35  
36  
37  
38  
39  
40  
41  
42  
43  
44  
45  
46  
47  
48  
49  
50  
51  
52  
53  
54  
55  
56  
57  
58  
59  
60

shows structure I is an octagonal mesh structures without wall ridges, and structure II is with double helix outer ridges on the basis of structure I. A hexagon honeycomb porous structure is used as the reference structure to investigate mechanical properties of novel bio-inspired structures. Moreover, the three structures have the same outer diameter, inner diameter and wall thickness. The parameters of these structures are presented in Figure 2.

**Figure 2.** Bio-inspired tubular structures: (a) represents structure I, structure II and honeycomb structure, respectively. (b) 3D renderings of the three structures. (c) represents two-dimensional stretched-out view of bio-inspired structure I, where  $K=6\text{mm}$ ,  $L=4.2\text{mm}$ . (d) represents top view of the bio-inspired II, where  $K=3\text{mm}$ ,  $L=2.12\text{mm}$ . (e) represents parameters of honeycomb structure

Figure 2c shows that the octagonal mesh of bio-inspired I are composed of the supporting struts with 0 degrees,  $\pm 45$  degrees and 90 degrees. Its structural cell is divided into four square small units (a, b, c, d) and the two of them located on the diagonal points are exactly the same (for example, unit a and d, unit b and c are the same, respectively). Moreover, each unit has four inclined supporting struts and each supporting rib is connected with an inclined supporting rib in the adjacent two units. One boundary strut of the small unit was divided into three line segments and which can be described as follows:

$$K = \sqrt{2}L$$

On the basis of bio-inspired structure I, a double helix outer ridge is added to the outer wall of the structure in bio-inspired structure II. Taking into account the size of

the entire structure and the outer spiral ridge, the width of supporting struts are halved and its number was doubled comparing with the bio-inspired I.

Previous studies have shown that honey combs (Figure 2b) have excellent mechanical properties with low weight (Martínez-Martín & Thrall, 2014; Bukner et al, 2015). In this paper, the honeycomb structure is selected as a reference structure to compare with the novel glass sponge-inspired structures.

### 3.2 Investigation of mechanical properties of the bio-inspired structures

Mechanical properties of the bio-inspired structures were analyzed using ANSYS Workbench 15.0 software and the stress distribution diagrams were also obtained. The material of the models is photosensitive resin, the same as the material used for 3D printing of structure samples. Material parameters provided by the supplier are shown in Table 1 and the main dimensions of the three structure models are designed the same in order to compare their mechanical properties under the same condition. Considering complexity of the structures, the FE models shown in Extended Data Fig. 5 were meshed with the element SOLID 187 in ANSYS Workbench, which is defined by ten nodes, each having 3 degrees of freedom, at the same time, large deformation is allowed in order to reduce simulation errors. The element size is approximately 1mm, according to the following mesh convergence study in which the force response curves are obtained with three different mesh sizes: 0.5mm, 1.0mm and 2.0 mm. It can be seen that the mesh size of 1.0mm and 0.5 mm are almost overlapped, demonstrating the simulation results are converged with a mesh size no larger than 1.0 mm. So, the characteristic mesh size of the structures is hence set to be 1.0 mm. The

1  
2  
3  
4  
5  
6  
7  
8  
9  
10  
11  
12  
13  
14  
15  
16  
17  
18  
19  
20  
21  
22  
23  
24  
25  
26  
27  
28  
29  
30  
31  
32  
33  
34  
35  
36  
37  
38  
39  
40  
41  
42  
43  
44  
45  
46  
47  
48  
49  
50  
51  
52  
53  
54  
55  
56  
57  
58  
59  
60

total number of nodes and elements for three FEA models are given in Table 2.

Table 1 Material property in FEM analysis

Parameters	Data
Density (g/cm <sup>3</sup> )	1.16
Young's modulus (Mpa)	1600
Poisson's ratio	0.4
Yield strength	380Mpa
Tangent modulus	38Mpa

Table 2 Number of nodes and elements of the proposed models

Types	Bio-inspired	Bio-inspired	Honeycomb
	Structure I	Structure II	structure
Nodes	512796	598515	774609
Elements	318832	360952	486632

Considering the possible application of the proposed bio-inspired structures to the robot arm for aerospace applications, the analysis are mainly focused on the axial compression, torsion, and cantilever bending ability of the bio-inspired structures.

The mechanical tests of the bio-inspired structures were performed on an electronic universal testing machine. The structure samples were fabricated using stereolithography 3D-printing technology (Form 2, USA). The material is photosensitive resin and the dimension sizes of the samples are the same as that of the corresponding FEM models (Figure 3). Considering the bio-inspired II is not suitable for the structure with outer skins in engineering applications because its double helix outer ridges lead to the weak connection to the outer skins and which will reduce the



mechanical properties of the whole structure. Therefore, we only tested and compared mechanical properties of the bio-inspired I with the honeycomb structure, at the same time, the experimental results demonstrated the accuracy and reliability of FEM analysis.

**Figure 3.** Bio-inspired lightweight structure I and honeycomb structure built by 3D printing

### 3.2.1 Compression performance

For compression, one end of the model is fixed with all six freedoms and the other end along the central axis is exerted with displacement loading step by step (step length is 0.6 mm and the total number is 20 steps). According to the simulation, the compression load-displacement curves of the three models are shown in Figure 4 and the LWN-C can be calculated in Table 3. It is indicated that bio-inspired II has not significantly improved the structural compression-bearing ability, but instead decreased LWN-C due to increased mass. However, LWN-C of the bio-inspired I and bio-inspired II are 47.6% and 41.3% higher than that of the honeycomb structure, respectively.

**Figure 4.** Compression displacement curves in FEA simulations of the three structures

Table 3 LWN-C of the three structures

Types	Bio-inspired I	Bio-inspired II	Honeycomb structure
Mass (g)	12.17	14.28	8.46
Compression load (N)	2010.6	2258.0	946.3
LWN-C (N/g)	165.2	158.1	111.9

Moreover, the quasi-static compression tests were performed, and the samples

1  
2  
3  
4  
5  
6  
7  
8  
9  
10  
11  
12  
13  
14  
15  
16  
17  
18  
19  
20  
21  
22  
23  
24  
25  
26  
27  
28  
29  
30  
31  
32  
33  
34  
35  
36  
37  
38  
39  
40  
41  
42  
43  
44  
45  
46  
47  
48  
49  
50  
51  
52  
53  
54  
55  
56  
57  
58  
59  
60

were fixed and loaded as the same as those in the simulation. The pressure head moved with a constant velocity of 2 mm/min, the reaction force was recorded and monitored by sensors, and the force–displacement curve was obtained as shown in Figure 5.

**Figure 5.** Compression force-displacement curves of bio-inspired structures, comparison was performed between FEM results and experimental results: (a) Bio-inspired I, (b) Honeycomb structure

It can be seen from Figure 5 that the curves at the first stage are almost linear and the results of finite element analysis at this stage are close to the experimental curves. Then, the curves change into nonlinear characteristics and the slope of the curves decreases slowly until the maximum yield stress is reached. After this point the structures are no longer able to carry the load. Figure 6 shows the differences of maximum compressive load between the analytical result and the experimental results, demonstrating the reliability of FEM analysis. According to the testing data, the LWN-C of the structures was calculated in Table 4. It can be seen that the LWN-C of bio-inspired I is 57.1% higher than that of honeycomb structure.

**Figure 6.** The differences of maximum compressive load between FEM and experimental results

Table 4 The LWN-C of the structures

Number	Types	Compression load (N)	Mass*(g)	Average value of LWN-C (N/g)
1	Bio-inspired I	1992.06	12.2	164.17±0.9
2	Bio-inspired I	1997.52	12.1	

3	Bio-inspired I	2035.18	12.4	
4	Honeycomb structure	863.02	8.5	
5	Honeycomb structure	918.31	8.5	104.56±3.3
6	Honeycomb structure	874.63	8.4	

Note: In this paper, mass of the structure is denoted as the mass of the porous part in the structure, the solid section at two ends is not included.

Figure 7 shows the numerical deformation modes of the structures under the compression load. It is indicated that the bio-inspired I featured significant plastic deformation before undergoing eventual fracture of the supporting struts (Figure 7(a)).

On a macroscopic scale, these deformations resulted in large-scale “bulging,” wherein the failure was appeared in the radial direction due to the strut fracture because the transverse plastic deformation of the structure mainly emerged when it reached the yield stress, and this deformation could be enlarged continuously. At the same time, it can be perceived from von Mises stress cloud figures of the structures that the equivalent stress was mainly located in the 90 ° and 45 ° supporting ribs, especially in the 90 ° supporting ribs, indicating that these supporting ribs play an important role in the bearing compression load. Figure 7(b) shows that the honeycomb structure undergoes large deformation under a compression load. Its maximum stress occurred at the longitudinal supporting rib, resulting in local burst damage. Additionally,

1  
2  
3  
4  
5  
6  
7  
8  
9  
10  
11  
12  
13  
14  
15  
16  
17  
18  
19  
20  
21  
22  
23  
24  
25  
26  
27  
28  
29  
30  
31  
32  
33  
34  
35  
36  
37  
38  
39  
40  
41  
42  
43  
44  
45  
46  
47  
48  
49  
50  
51  
52  
53  
54  
55  
56  
57  
58  
59  
60

according to the compression fracture pictures of both structures (Figures 5(a) and (b)), the main fracture happened to 90° supporting ribs with a smooth fracture cross-section, which is in accordance with the analytical results. The 90° supporting ribs mainly bear the compression, tensile, and bending loads, which is in accordance with the findings obtained by Markus et al (Markus et al, 2006).

**Figure 7.** Diagrams of numerical deformation mode under compression load: (a) bio-inspired I and (b) honeycomb structure

**3.2.2 Torsion performance**

For torsion analysis, one of the model end is fixed for all six degrees of freedom (DOFs) and the other end along central axis is exerted with torsion angle load step by step (step angle is 3° and the total number were 15 steps). Moreover, in order to further study the torsion behavior of bio-inspired II, it is applied by clockwise and counterclockwise torsion load. The torsion load - displacement curves of the three models are shown in Figure 8. The LWN-T of the three structures are calculated in Table 5, which indicated that LWN-T of bio-inspired structure II is the greatest and whose torsion-bearing abilities are exactly the same under the loads in two opposite directions (clockwise and counterclockwise). It also can be seen that the special outer spiral ridge can not only bear the bi-directional torsion load, but also improve the torsion bearing ability and increase the LWN-T coefficient. Moreover, it is indicated that LWN-T of bio-inspired I and bio-inspired II are 222.8% and 242.1% higher than that of honeycomb structure, respectively.

**Figure 8.** Torsion load displacement curve in FEA simulations of the three structures

Table 5 LWN-T of the three structures

Types	Bio-inspired I	Bio-inspired II (clockwise)	Bio-inspired II (counterclockwise)	Honeycomb structure
Mass (g)	12.17	14.28	14.28	8.46
Torsion load (N•m)	22.34	27.81	27.81	4.83
LWN-T (N m/g)	1.84	1.95	1.95	0.57

The torsion test was performed by torsion testing machine (QBN100-L100). The load and torsion angle data of the experiment instrument was cleared before the tests. Then, the load velocity of 5 %/min was set to carry out the torsion tests and the torsion-angle curves were obtained. The FEM results and experimental results are compared in Figure 9. It can be seen from Figure 9 that the experimental results are in good accordance with the analysis results in the linear-elastic stage. Figure 10 shows the differences of maximum torsion load between FEM and experimental results. These results indicate that the simulation results are very close with experimental results. Table 6 shows the LWN-T of two kinds of structures, and LWN-T of bio-inspired I is 257.4% higher than that of honeycomb structure.

**Figure 9.** Torsion force-angle curves of bio-inspired structures, comparison was performed between FEM results and experimental results: (a) Bio-inspired I. (b) Honeycomb structure

**Figure 10.** The differences of maximum torsion load between FEM and experimental results

Table 6 The LWN-T numbers of the bio-inspired structures and the honeycomb structure

Number	Types	Torsion load (N•m)	Mass* (g)	Average value of LWN-T (N•m /g)
1	Bio-inspired I	23.141	11.8	1.93±0.04
2	Bio-inspired I	23.784	12.2	
3	Bio-inspired I	22.717	12.1	
4	Honeycomb structure	4.672	8.7	0.54±0.01
5	Honeycomb structure	4.467	8.3	
6	Honeycomb structure	4.652	8.4	

Figures 11(a) and (b) indicate that the stress of the bio-inspired I is mainly concentrated on the  $\pm 45^\circ$  supporting ribs, and the honeycomb structure mainly appears on the  $90^\circ$  supporting ribs. Figures 16 (a, b) shows that the fracture of both structures occurred at  $\sim 45^\circ$  under torsion load with the domination of shear failure. This is because the maximum shear emerged at  $45^\circ$  (maximum shear stress is obtained as  $\tau_{\max} = \frac{\sigma}{2} \sin(2\alpha) \Big|_{\alpha=45^\circ} = \frac{\sigma_s}{2}$ ). The fracture modes of the samples also show good agreement with the simulation results.

**Figure 11.** Diagrams of numerical deformation mode under torsion load: (a) bio-inspired I and (b) honeycomb structure

### 3.2.3 Bending performance

For bending analysis, one end of the model is fixed with all six freedoms, and the other end is pressed with a pressure head vertically step by step (step length is 3 mm and the total number were 15 steps). Material properties of the pressure head are shown in Table 7. The contact between the structural model and the pressure head is defined as frictionless and the contact behavior is set as “symmetric” in definition for Ansys Workbench 15.0.

Table 7 Material properties of the pressure head

Material	Diameter	Young's modulus	Compression yield strength
Steel	10 mm	200 GPa	250 MPa

To compare the bending strengths of the three structures, their bending force-displacement curves are shown in Figure 12. Table 8 shows that LWN-B of bio-inspired I and bio-inspired II increased 96.0% and 81.5% respectively comparing with that of honeycomb structure.

**Figure 12.** Bending load displacement curves in FEA simulations of the three structures

Table 8 LWN-B of the three structures

Types	Bio-inspired I	Bio-inspired II	Honeycomb structure
Mass (g)	12.17	14.28	8.46
Bending load (N)	155.74	169.15	55.27
LWN-B (N/g)	12.80	11.85	6.53

For bending test, the special sample holding device was installed and fixed on the platform of the test machine. After the sample was fixed by one end, the pressure head began to gradually approach to the sample till they contacted each other at the

1  
2  
3  
4  
5  
6  
7  
8  
9  
10  
11  
12  
13  
14  
15  
16  
17  
18  
19  
20  
21  
22  
23  
24  
25  
26  
27  
28  
29  
30  
31  
32  
33  
34  
35  
36  
37  
38  
39  
40  
41  
42  
43  
44  
45  
46  
47  
48  
49  
50  
51  
52  
53  
54  
55  
56  
57  
58  
59  
60

other end of the sample without any preload, then the pressure head continued to move at the speed of 2mm/min. Obviously, different load position on these structures can affect their bending properties. So, the directionality and position of the load on these structures are considered in bending test. The load condition is defined as load 1, load 2 and load 3 shown in Figure 13a, and honeycomb structure is defined as load 1 and load 2 shown in Figure 13b. It can be seen that there isn't much difference between the results with different load conditions. Additionally, the honeycomb structure is highly symmetrical, the load position has little effect on the maximum bending load capacity. Figure 14 shows that the differences of maximum bending load between the FEM results and experimental results. Table 9 shows the maximum bending load and the LWN-B of the structures.

**Figure 13.** Comparison between FEM analysis and experimental results under the bending force for two structures: (a) Bio-inspired I. Load 1, load 2 and load 3 represent different load position on Bio-inspired I in the testing, respectively \*. The simulation results represent load condition 2. (b) Honeycomb structure. Load 1 and load 2 represent different load position on honeycomb structure, respectively. The simulation results represent load condition 1. Note\*: In our bending experiments, the force is loaded in the three difference positions at the solid end of the samples, the red dotted line, purple dotted line and blue dotted line are the lines which are through the three different force points respectively and paralleled to the axis of the tube, demonstrating the corresponding grid part of the tube

**Figure 14.** The differences of maximum bending load between FEM and experimental values



434

Table 9 The LWN-B of the structures

Number	Types	Bending load (N)	Mass* (g)	Average value of LWN-B (N/g)
1	Bio-inspired I	146.19	12.2	12.04±0.35
2	Bio-inspired I	144.21	12.3	
3	Bio-inspired I	151.52	12.2	
4	Honeycomb structure	52.48	8.5	6.22±0.22
5	Honeycomb structure	51.27	8.5	
6	Honeycomb structure	54.97	8.5	

435 It can be seen that the LWN-B number of bio-inspired I is almost 2 times of  
436 honeycomb structure. As shown in Figures 15(a) and (b), the maximum stress of both  
437 structures appeared at their fixed ends under the bending load, which is the  
438 combination of normal stress and shear stress, finally caused the local instability and  
439 fracture. The images of bending fracture— Figures 13 (a) and (b) — show that the  
440 bio-inspired I is broken along the 45 ° or 90 ° supporting ribs when it approaches the  
441 strength limitation. However, the honeycomb structure show severe plastic  
442 deformation and has a uniform fracture at the 90 ° supporting ribs. Previous  
443 experimental results have supported these analyses. The network structure and  
444 octagon mesh of glass sponges are formed between the ±45 ° supporting ribs and the

1  
2  
3  
4  
5  
6  
7  
8  
9  
10  
11  
12  
13  
14  
15  
16  
17  
18  
19  
20  
21  
22  
23  
24  
25  
26  
27  
28  
29  
30  
31  
32  
33  
34  
35  
36  
37  
38  
39  
40  
41  
42  
43  
44  
45  
46  
47  
48  
49  
50  
51  
52  
53  
54  
55  
56  
57  
58  
59  
60

boundary struts, which mainly bear the torsion and shear load and prevent structural deformation. In addition, the  $\pm 45^\circ$  ribs can also improve the antitorsion ability in two directions and effectively prevent the failure of the structure from the elliptical change of the structure's cross-section when bearing the torsion or bending loads (Aizenberg et al, 2005; Weaver et al, 2007). Bacheva et al. (Bacheva et al, 2011) has carried out a detailed study of the unique lattice structure and pointed out that  $\pm 45^\circ$  ribs are interwoven with horizontal and vertical ribs, and lattices with open and closed cells formed to provide a support for the main skeleton, therefore improved the ability to bear the overall bending, shearing, and torsion. Such a configuration represents an optimized and lightweight structural design concept. This research on the proposed thin-walled structures inspired by glass sponge demonstrates its excellent mechanical properties and provides a potential application in the aerospace.

**Figure 15.** Diagrams of numerical deformation mode under bending load: (a) bio-inspired I and (b) honeycomb structure

### 3.3 Parameter optimization of the bio-inspired structure

Due to its superior mechanical properties, bio-inspired I was chosen as the model for further parameter optimization. Here, the optimization is obtained under the assumption that the structure is only subjected to the compression load. The flowchart of parameter optimization based on the response surface method can be summarized in Fig. S6.

#### 3.3.1 Experimental samples

The objective of optimization is to maximum the LWN without changing the

structures formations. According to the characteristics of the structure and the constraint relationship between the parameters, the variation range of parameters is determined 10% to 20%. The design variables and constraints are given in Fig. S7 and Table 10. Optimization objective and parameters are presented as below:

Max LWN

$$S.T \begin{cases} 40^{\circ} \leq DS\_Angle \leq 50^{\circ} \\ 2.3 \leq DS\_Width\ 1 \leq 2.9 \\ 2.3 \leq DS\_Width\ 2 \leq 2.9 \\ 2.3 \leq DS\_Width\ 3 \leq 2.9 \end{cases}$$

Table 10 Variables and constraints

Variables	Minimum	Maximum
DS_Angle ( ° )	40 °	50 °
DS_Width 1 (mm)	2.3	2.9
DS_Width 2 (mm)	2.3	2.9
DS_Width 3 (mm)	2.3	2.9

The optimization design is performed using Design Exploration in ANSYS Workbench 15.0. Latin Hypercube Sampling (LHS) design is applied to determine numbers of experimental samples. Sample points and its response value are shown in table S1.

### 3.3.2 Fitting and forecasting analysis

According to the above sample points, kriging method is used to generate the response surface and the relations between geometric structure parameters and compression load capacity are shown in Fig. S8.

In order to improve the fitting and forecasting precision, BP and GA-BP models are proposed. In addition, four input variables are obtained from Table 11 such as,

1  
2  
3  
4  
5  
6  
7  
8  
9  
10  
11  
12  
13  
14  
15  
16  
17  
18  
19  
20  
21  
22  
23  
24  
25  
26  
27  
28  
29  
30  
31  
32  
33  
34  
35  
36  
37  
38  
39  
40  
41  
42  
43  
44  
45  
46  
47  
48  
49  
50  
51  
52  
53  
54  
55  
56  
57  
58  
59  
60

DS\_Angle, DS\_Width 1, DS\_Width 2 and DS\_Width 3. Compression load is used as an output variable. Total data consisted of 40 samples in Table 11. From these data, BP and GA-BP models are trained by the same 20 groups of samples and are tested by the other 20 groups of samples. The values of all parameters of the selected samples in training set and validation set are normalized at  $[-1, 1]$  to make the model quickly converge. The parameters of the models are listed in table 11.

Table 11 Parameters of the models

Algorithm	Name	value
BP	Network structure	4-5-1
	Transfer function	Logsig, Purelin
	Training function	Levenberg-Marquardt
	Learning function	learngdm
	Number of iterations	1000
	Learning ratio	0.1
	Performance error	0.00001
GA	Population size	10
	Evolutional generation	60
	Population type	Real number
	Selection function	Roulette
	Crossover probability	0.4
	Mutation probability	0.1

Fig. S9 (a) and (c) indicated that GA-BP outputs are closer to the expected output than BP outputs. Fig.S9 (b) and (d) shows the convergence curve of the training set of BP and GA-BP model. It is found that the mean squared error (MSE) of BP is 0.029737 at epoch 2, while GA is 0.005677 at epoch 26. Fig. S10 illustrates the correlation between the training output and the expected output, where  $R^2 \in [0,1]$  is

the correlation coefficient. The closer the value of  $R^2$  is to 1, the better the correlation between the training output and the expected value. It should be noted that  $R^2=0$  indicates that the input and output of the neural network is selected inappropriately, and the neural network predictor must be redesigned. From Fig. S10, it can be seen that the training output and the expected output of GA-BP model are better correlated than those of BP model.

Fig. S11 (a) shows the fitness function of GA, it can be seen that when the number of evolution generation reaches 20 the best fitness function value becomes stable, indicating that optimal solution of GA has been approximately obtained. Fig. S11 (b) shows the weights and thresholds of the optimal individual. Absolute error curves of GA-BP and BP are presented in Fig. S11 (d) and (e), respectively. Absolute error and relative error can be defined as follows:

$$E_1 = \hat{Y} - Y \quad (19)$$

$$E_2 = \left( \frac{\hat{Y} - Y}{Y} \right) \times 100\% \quad (20)$$

Where  $\hat{Y}$  is the predictive value,  $Y$  is the expected value,  $E_1$  is the absolute error,  $E_2$  is the relative error.

From Fig. S11 (b) it can be seen that the maximum absolute error of the BP and GA-BP model is 105 and 48 respectively, indicating GA-BP model prediction ability is better than that of pure BP method. Fig. S11 (c) and (f) shows the relative error curve of GA-BP and BP model, indicated that the maximum relative error of the GA-BP and BP model is 1.7%, 3.8% respectively. Therefore, the performance of the

1  
2  
3  
4  
5  
6  
7  
8  
9  
10  
11  
12  
13  
14  
15  
16  
17  
18  
19  
20  
21  
22  
23  
24  
25  
26  
27  
28  
29  
30  
31  
32  
33  
34  
35  
36  
37  
38  
39  
40  
41  
42  
43  
44  
45  
46  
47  
48  
49  
50  
51  
52  
53  
54  
55  
56  
57  
58  
59  
60

GA-BP model is better than BP due to its advantage in the global optimal parameters selection, which means that the GA-BP model has a higher accuracy after training and can be used to fit and predict the compression capacity of the bio-inspired structure very well.

**3.3.3 Optimization results**

Screening method is selected as optimization method to generate 2000 samples, and three optimization schemes are determined in process of approaching the objective using the response surface method, as shown in table 12.

Table 12 Optimization schemes

Design variables and goals	Optimization scheme A	Optimization scheme B	Optimization scheme C
DS_Angle ( ° )	49.1314 °	49.8478 °	48.1162 °
DS_Width 1 (mm)	2.88	2.9	2.86
DS_Width 2 (mm)	2.68	2.86	2.52
DS_Width 3 (mm)	2.86	2.9	2.81
Max Compression load (N)	3095	3118.7	3059.1
LWN-C (N/g)	227.51	231.59	214.91

Table 13 presents the fitting results and relative errors of the three optimization schemes determined by 3 algorithms, proving the optimization scheme B is the best solution. It can be observed that GA-BP model has the higher accuracy than other methods.

Table 13 Fitting results and relative errors by 3 methods

		Response surface	BP	GA-BP	Numerical
Max Compression load (N)	scheme A	3095	2952.4	2713.3	2797.4
	Relative error	10.6%	5.5%	3%	
	scheme B	3118.7	2935.2	2803.6	2844.3
	Relative error	9.6%	3.2%	1.4%	
	scheme C	3059.1	2943.7	2821.0	2785.6
	Relative error	9.8%	5.7%	1.3%	

From table 14 it can be seen that through optimization design, the compression load and LWN-C of the bio-inspired I are dramatically increased by 41.47% and 30.85%, respectively. Also, the other two mechanical properties discussed in this paper and the corresponding LWN numbers of the structure are improved to some extension.

Table 14 Comparison between the initial model and optimization model

	Initial structure	Optimized structure	Percentage increase
Compression load (N)	2010.6	2844.3	41.47%
Torsion load (N)	22.34	27.109	21.35%
Bending load (N)	155.74	200.98	29.05%
LWN-C (N/g)	165.2	211.22	27.68%
LWN-T (N m/g)	1.84	2.01	9.2%
LWN-B (N/g)	12.8	14.92	16.56%

### 3.3.4 Discussion

In the course of evolution, nature has produced extremely energy-saving designs by natural selection as the best strategy in the continuous struggle for survival of the

1  
2  
3  
4  
5  
6  
7  
8  
9  
10  
11  
12  
13  
14  
15  
16  
17  
18  
19  
20  
21  
22  
23  
24  
25  
26  
27  
28  
29  
30  
31  
32  
33  
34  
35  
36  
37  
38  
39  
40  
41  
42  
43  
44  
45  
46  
47  
48  
49  
50  
51  
52  
53  
54  
55  
56  
57  
58  
59  
60

species (Maier et al, 2013). The glass sponge is a successful evolution of thin-walled structures; it is made up of an interconnected network of struts or plates forming the edges and faces of the structure cells, and it possesses excellent mechanical behaviors.

Lightweight thin-walled structures are suitable for multifunctional applications that require not only light weight but also high strength. Different thin-walled structures inspired by nature, such as bamboo (Xu et al, 2014; Song et al, 2017; Zhao et al, 2019), wild horsetails (Yin et al, 2015), dutch rush (Speck et al, 2004), squares (Yang & Qi, 2013), and hedgehog spines (Dawson & Gibson, 2007) have already been investigated. Based on our previous work, thin-walled structures inspired by the glass sponge, which are used as good core of the sandwich structures, have been investigated by employing experimental, analytical, and numerical methods. Additionally, the lightweight number is used to evaluate the lightweight efficiency of the bio-inspired structures. The results show that, in many respects, the novel structure has better mechanical properties than a honeycomb structure. This shows that, with some refinement, the proposed thin-walled structures can be used to produce lighter parts with less material in engineering applications, such as in the aerospace industry, vehicles, and ships, ect.

This study proposed the lightweight structure inspired by the glass sponge and investigated its mechanical properties in detail, as well as optimization. The purpose is to present new lightweight thin-walled structures and to provide some new biomimetic ideas in designing and developing lightweight structures.

563



## Conclusions

The lightweight thin-walled structure inspired by glass sponges was proposed and its mechanical properties were investigated numerically and experimentally in this study. Finally, the proposed bio-inspired structure I was optimized. Within the limitations of the study, the following conclusions can be drawn:

(1) The morphology of the specimen was observed using the super depth of field microscope. Based on its morphological characteristics, two novel bio-inspired thin-walled structures were proposed.

(2) Due to the bio-inspired I is more suitable for the sandwich structure with outer skins in engineering. Therefore, we only tested and compared mechanical properties of the bio-inspired with the honeycomb structure, at the same time the experimental results demonstrated the accuracy and reliability of FEM analysis. FE analysis of the bio-inspired structures showed that, comparing with the honeycomb structure, the LWN-C, LWN-T and LWN-B of the bio-inspired I are 47.6%, 222.8% and 96.0% higher respectively, and the values of bio-inspired II are 41.3%, 242.1% and 81.5% higher respectively. In addition, the structure samples were fabricated using SLA 3D printing technology and its mechanical properties were tested under compression, torsion and cantilever bending loads, respectively, the results demonstrated the reliability of FEA results.

(3) Response surface method was used to optimize the proposed structure without changing the structures formations. Comparing with the initial structure, the LWN-C, LWN-T and LWN-B of optimized structure increased 27.68%, 9.2% and

1  
2  
3  
4 586 16.56%, respectively.  
5

6 587 (4) The proposed structures were optimized by using the response surface, BP  
7  
8  
9 588 and GA-BP method. The results indicated the performance of the GA-BP model was  
10  
11  
12 589 better than BP, which has a high accuracy and can be used to predict the mechanical  
13  
14  
15 590 properties of the structures very well.

16  
17 591 (5) The results showed that the proposed structures inspired by glass sponges can  
18  
19  
20 592 be used to produce lighter structure with less material and still keep the excellent  
21  
22  
23 593 mechanical properties, which has great potential in the engineering applications, such  
24  
25 594 as aerospace, vehicles and ships.

26  
27 595  
28  
29  
30 596  
31  
32 597  
33  
34  
35 598  
36  
37 599  
38  
39  
40 600  
41  
42  
43 601  
44  
45 602  
46  
47  
48 603  
49  
50 604  
51  
52  
53 605  
54  
55  
56 606  
57  
58  
59  
60

## Acknowledgments

This work was supported by the National Natural Science Foundation of China [grant numbers 51875282, 51175249 and 51475230]; National Defense Basic Scientific Research Project [JCKY2018605C010]; Postgraduate Research & Practice Innovation Program of Jiangsu Province (KYLX16\_0323).

## Conflict of Interests

The authors declare that there is no conflict of interests regarding the publication of this article.

## References

- [1] Aizenberg J and Hendler G 2004 Designing efficient microlens arrays: lessons from Nature *J. Mater. Chem.* **14**, 2066-2072.
- [2] Aizenberg J, Sundar VC, Yablon AD, Weaver JC and Chen G 2004 Biological glass fibers: Correlation between optical and structural properties *P. Natl. Acad. Sci. USA.* **101**, 3358.
- [3] Aizenberg J, Weaver JC and Thanawala MS 2005 Skeleton of *Euplectella* sp.: structural hierarchy from the nanoscale to the macroscale *Science* **309**, 275-278.
- [4] Bacheva D, Elsayed MSA and Trask RS 2011 The skeleton of *Euplectella aspergillum* as foundation for the development of novel composite aerospace structures: 18th International Conference on Composite Materials, Jeju Island, Korea,
- [5] Bukner S, Farid D, Ding L and Jason M 2015 Bio-inspired Design to Support Reduced Energy Consumption Via the 'Light Weighting' of Machine System Elements *Int. J. Model. Optimization.* **5**, 82-89.
- [6] Chen Q, Shi Q, Gorb SN and Li ZY 2014 A multiscale study on the structural and mechanical properties of the luffa sponge from *Luffa cylindrica* plant *J. Biomech.* **47**, 1332-1339.
- [7] Chen JX, Xu M, Okabe Y, Guo ZS and Yu XD 2017a Structural characteristics of the core layer and biomimetic model of the ladybug forewing *Micron* **101**, 156-161.
- [8] Chen JX, Zhang XM, Okabe Y, Saito K, Guo ZS and Pan LC 2017b. The Deformation Mode and Strengthening Mechanism of Compression in the Beetle Elytron Plate. *Mater. Design.* **131**, 481-486.
- [9] Drozdov AL and Karpenko AA 2011 Structural Arrangement and Properties of Spicules in Glass Sponges *Isrn. Mater. Sci.* **2011**, 1-8.
- [10] Dohrmann M, Kelley C, Kelly M, Pisera A, Hooper J and Reiswig H 2017. An integrative systematic framework helps to reconstruct skeletal evolution of glass sponges (Porifera, Hexactinellida). *Front. Zool.* **14**, 18.
- [11] Dawson MA and Gibson LJ 2007. Optimization of cylindrical shells with compliant cores. *Int. J. Solids. Struct.* **14**, 1145-1160.
- [12] Guo C, Song WW and Dai ZD 2012 Structural design inspired by beetle elytra and its mechanical properties. *Chinese. Sci. Bull.* **57**, 941-947.
- [13] Jiao H, Zhang Y and Chen W 2010 The Lightweight Design of Low RCS Pylon Based on Structural Bionics *J. Bionic. Eng.* **07**, 182-190.
- [14] Li L, Guo C, Li X, Xu S and Han C 2017 Microstructure and mechanical properties of rostrum in *Cyrtotrachelus longimanus* (Coleoptera: Curculionidae) *Anim. Cells. Syst.* **21**, 199-206.
- [15] Li SH, Zeng QY, Xiao YL, Fu SY and Zhou BL 1995 Biomimicry of bamboo bast fiber with engineering composite materials *Mater. Sci. Eng. C-Biomim. Mater. Sensors. Syst.* **3**, 125-130.
- [16] Leys SP, Kamarul AZ and Boury-Esnault N 2016 Three-dimensional fate mapping of larval tissues through metamorphosis in the glass sponge *Oopsacas minuta* *Invertebr. Biol.* **135**, 259-272.
- [17] Leys SP, Mackie GO and Reiswig HM 2007 The Biology of Glass Sponges *Adv. Mar. Biol.* **52**, 1-145.
- [18] Monn MA, Weaver JC, Tianyang Z, Aizenberg J and Kesari H 2015 New functional insights

- into the internal architecture of the laminated anchor spicules of *Euplectella aspergillum* *P. Natl. Acad. Sci. USA*. **112**, 4976.
- [19] Maier M, Siegel D, Thoben KD, Niebuhr N and Hamm C 2013 Transfer of Natural Micro Structures to Bionic Lightweight Design Proposals *J. Bionic. Eng.* **10**, 469-478.
- [20] Martínez-Martín FJ and Thrall AP 2014 Honeycomb core sandwich panels for origami-inspired deployable shelters: Multi-objective optimization for minimum weight and maximum energy efficiency *Eng. Struct.* **69**, 158-167.
- [21] Markus M, Thomas S and Olga S 2006 Heinrich, Biomimetics and technical textiles: solving engineering problems with the help of nature's wisdom *Am. J. Bot.* **93**, 1455-1465.
- [22] Parameswaran N and Liese W 1976 On the fine structure of bamboo fibres *Wood. Sci. Technol.* **10**, 231-246.
- [23] Smith CW, Herbert R, Wootton RJ and Evans KE 2000 The hind wing of the desert locust. II: Mechanical properties and functioning of the membrane *J. Exp. Biol.* **203**, 2933-2943.
- [24] Sun JY and Bhushan B 2012 The structure and mechanical properties of dragonfly wings and their role on flyability *CR. Mecanique.* **340**, 3-17.
- [25] Song J, Wang H and Gai H 2017 Bionic Optimization Design of Thin-walled Energy Absorption Tube Inspired by Bamboo Structure *Manned. Spaceflight.* **4**, 473-481. (Chinese)
- [26] Speck T, Masselter T, Prüm B, Speck O, Luchsinger R and Fink S 2004 Plants as concept generators for biomimetic lightweight structures with variable stiffness and self-repair mechanisms *J. Bionic. Eng.* **1**, 199-205.
- [27] Tong J, Xu S, Chen DH and Li M 2017 Design of a Bionic Blade for Vegetable Chopper *J. Bionic. Eng.* **14**, 163-171.
- [28] Wang XC, Shi F, Yu L and Li Y 2013 Analysis of 43 cases of neural network by MATLAB Beijing University of Aeronautics and Astronautics Press, Beijing.
- [29] Weaver JC, Aizenberg J and Fantner GE 2007 Hierarchical assembly of the siliceous skeletal lattice of the hexactinellid sponge *Euplectella aspergillum* *J. Struct. Biol.* **158**, 93-106.
- [30] Xu S, Zou M and Wei C 2014 Axial crashworthiness analysis and optimization of a bionic thin-walled tube based on bamboo structure *J. Tsinghua. University.* **54**, 299-304. (Chinese)
- [31] Yu GZ, Chou DT, Hong D and Kumta PN 2017 Biomimetic Rotated Lamellar Plywood Motifs by Additive Manufacturing of Metal Alloy Scaffolds for Bone Tissue Engineering *ACS. Biomater. Sci. Eng.* **3**, 648-657.
- [32] Yang ZX and Dai ZD 2010 Morphology and mechanical properties of *Cybister elytra* *Sci. Bull.* **55**, 771-776.
- [33] Yin H, Xiao Y, Wen G, Qing Q and Wu X 2015 Crushing analysis and multi-objective optimization design for bionic thin-walled structure *Mater. Design.* **87**, 825-834.
- [34] Yang S and Qi C 2013 Multiobjective optimization for empty and foam-filled square columns under oblique impact loading *Int. J. Impact. Eng.* **54**, 177-191.
- [35] Zhao L, Ma JF, Wang T and Xing DH 2010 Lightweight design of mechanical structures based on structural bionic methodology *J. Bionic. Eng.* **7**, 224-231.
- [36] Zhao L, Ma JF, Chen WY and Guo HL 2011 Lightweight design and verification of gantry machining center crossbeam based on structural bionics *J. Bionic. Eng.* **8**, 201-206.
- [37] Zhang XM, Chen JX, Okabe Y, Xie J and Zhang ZJ 2017. Compression properties of metal beetle elytron plates and the elementary unit of the trabecular-honeycomb core structure *J. Sandw Struct. Mater.* <https://www.researchgate.net/publication/318880007>.

1  
2  
3  
4  
5  
6  
7  
8  
9  
10  
11  
12  
13  
14  
15  
16  
17  
18  
19  
20  
21  
22  
23  
24  
25  
26  
27  
28  
29  
30  
31  
32  
33  
34  
35  
36  
37  
38  
39  
40  
41  
42  
43  
44  
45  
46  
47  
48  
49  
50  
51  
52  
53  
54  
55  
56  
57  
58  
59  
60

[38] Zou M, Xu SC, Wei CG, Wang HX and Liu ZZ 2016 A bionic method for the crashworthiness design of thin-walled structures inspired by bamboo *Thin. Wall. Struct.* **101**, 222-230.

[39] Zhao C, Ren L, Song Z, Deng LH and Liu QP 2019 A study on the tubular composite with tunable compression mechanical behavior inspired by wood cell *J. Mech. Behav. Biomed.* **89**, 132-142.

754 **Figure legends**

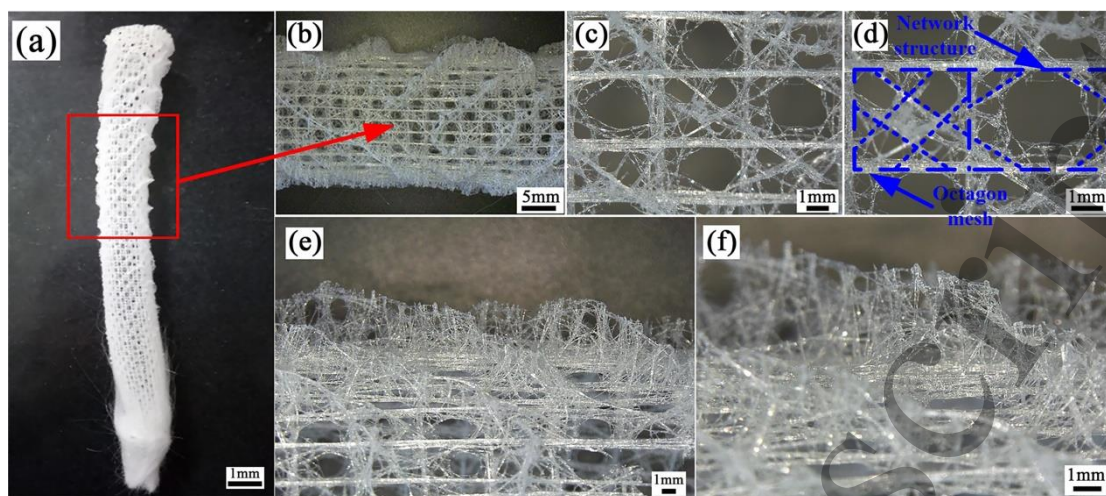


**Figure 1.** Macrostructures and microstructures of the sample: (a) specimen, (b) a part of the specimen, (c) the macrostructures and microstructures, (d) details of the macrostructures and microstructures in an enlarged view (blue line represents the main skeleton including network structure and octagon mesh), (e) wall ridges, and (f) details of the wall ridges

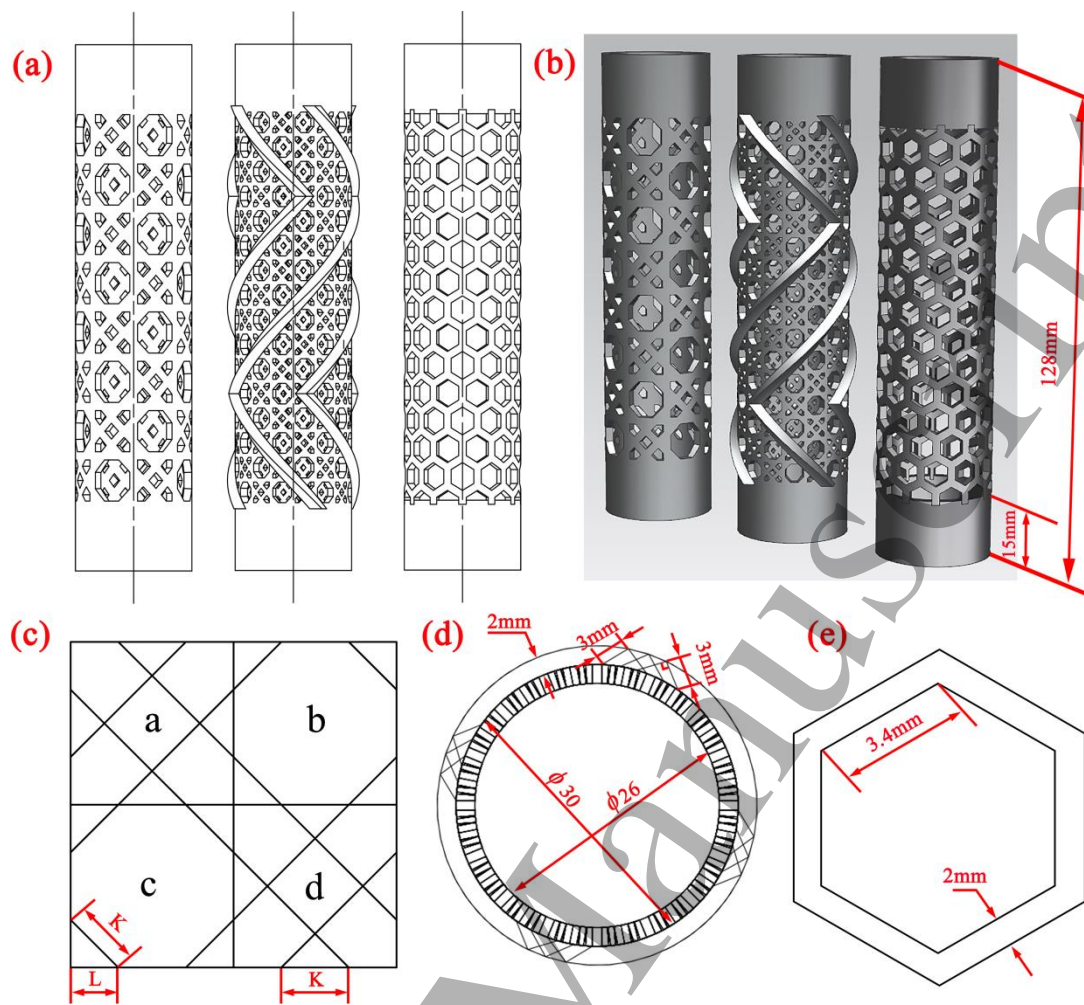


**Figure 2.** Bio-inspired tubular structures: (a) represents structure I, structure II and honeycomb structure, respectively. (b) 3D renderings of the three structures. (c) represents two-dimensional stretched-out view of bio-inspired structure I, where  $K=6\text{mm}$ ,  $L=4.2\text{mm}$ . (d) represents top view of the bio-inspired II, where  $K=3\text{mm}$ ,  $L=2.12\text{mm}$ . (e) represents parameters of honeycomb structure



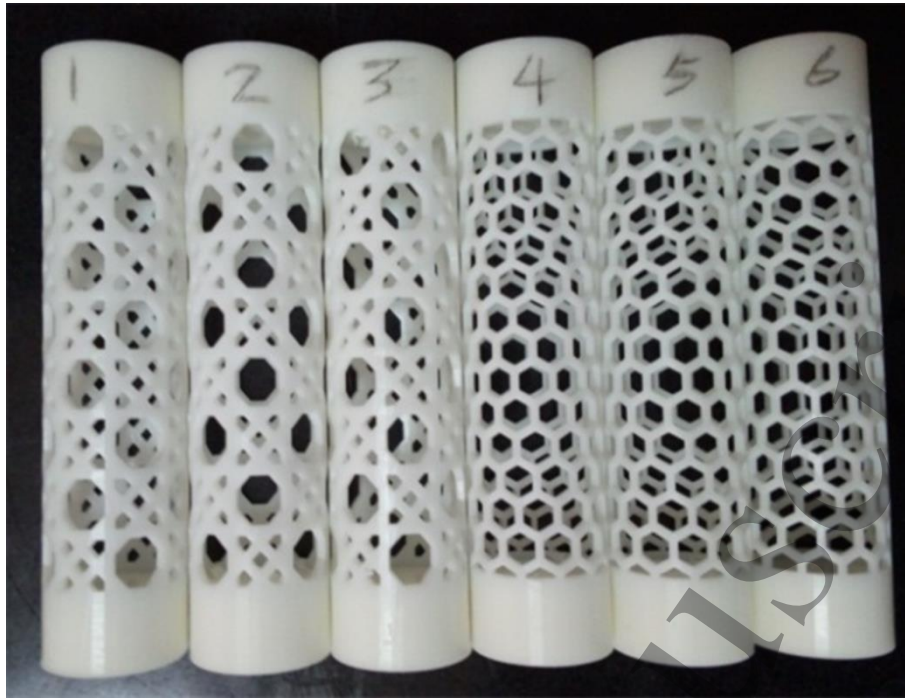


**Figure 3.** Bio-inspired lightweight structure I and honeycomb structure built by 3D printing

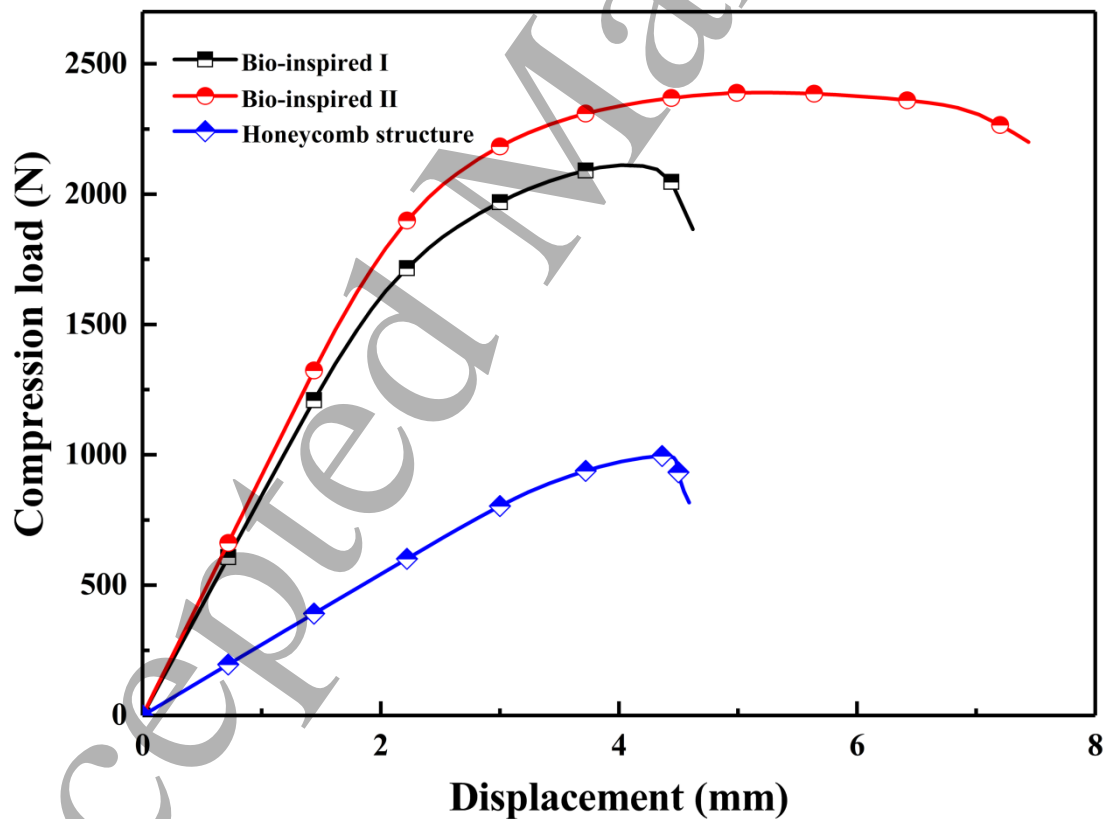


**Figure 4.** Compression displacement curves in FEA simulations of the three structures

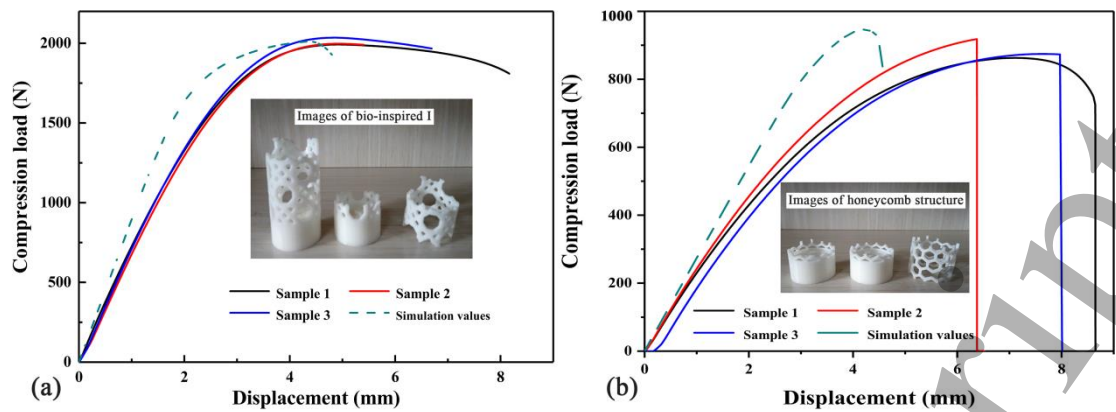


**Figure 5.** Compression force-displacement curves of bio-inspired structures, comparison was performed between FEM results and experimental results: (a) Bio-inspired I, (b) Honeycomb structure

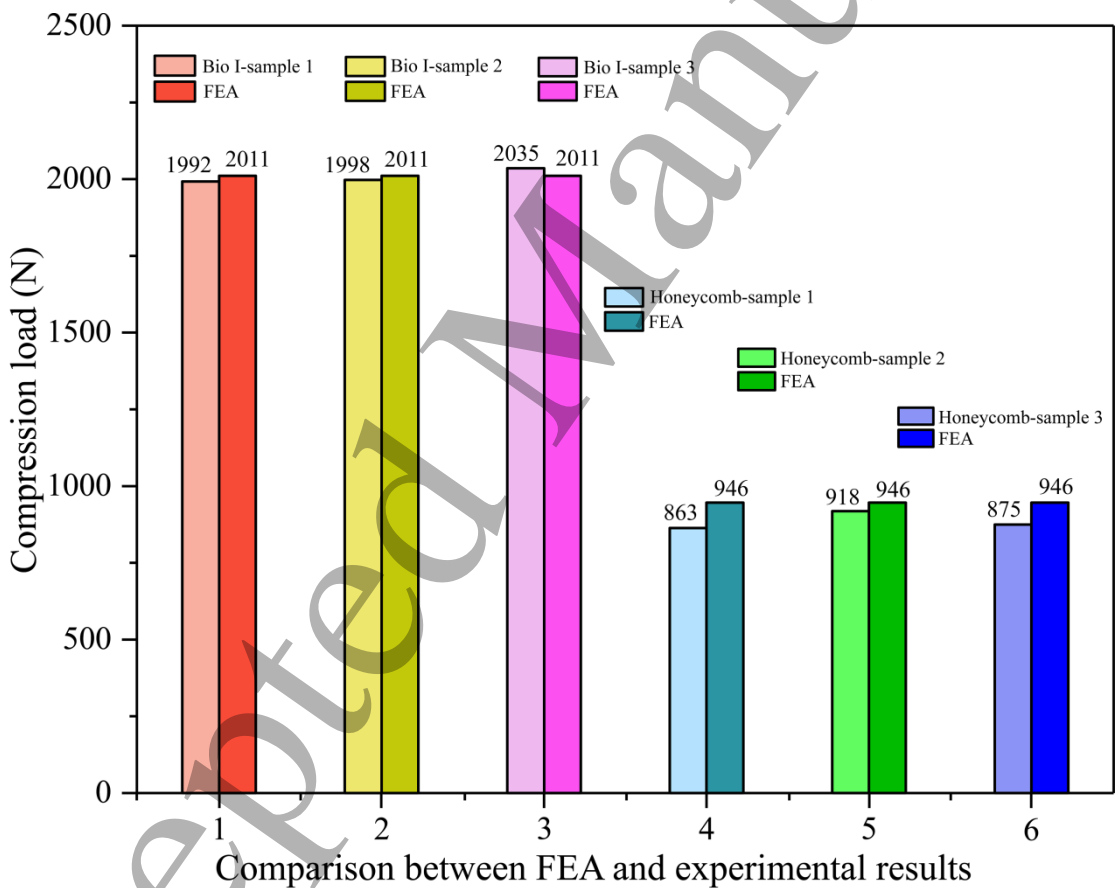


**Figure 6.** The differences of maximum compressive load between FEM and experimental results

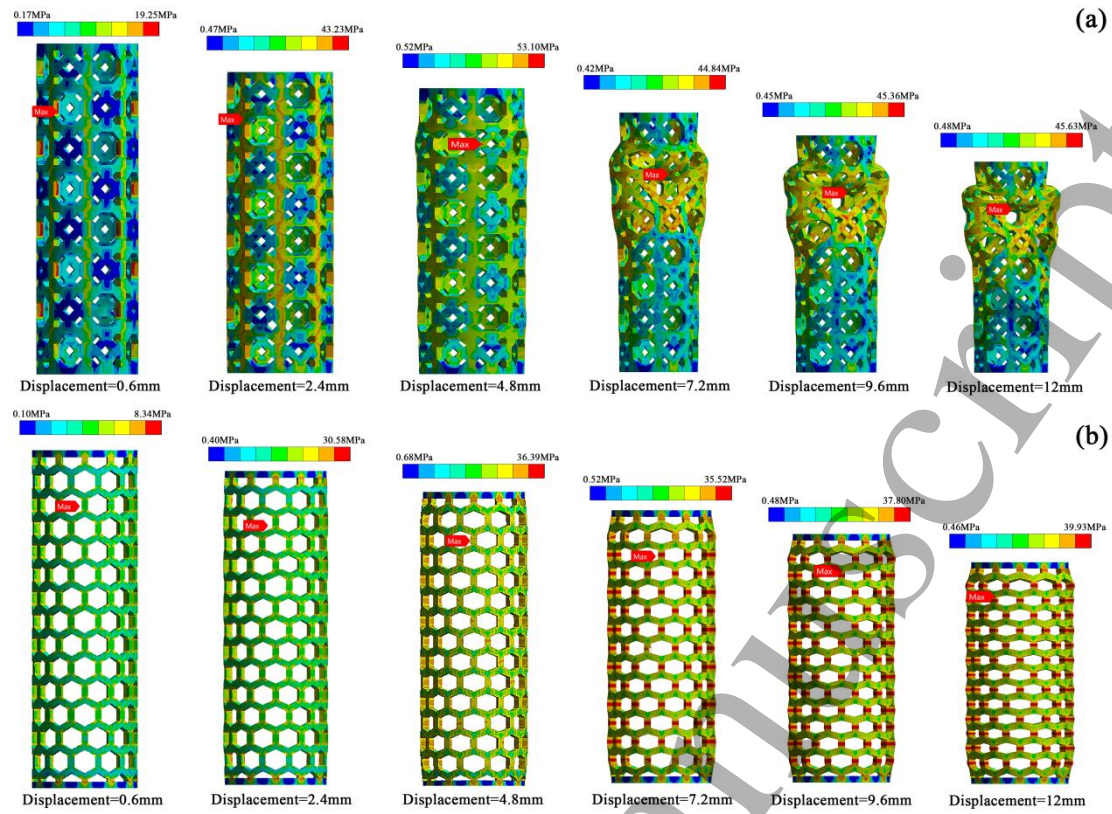


**Figure 7.** Diagrams of numerical deformation mode under compression load: (a) bio-inspired I and (b) honeycomb structure

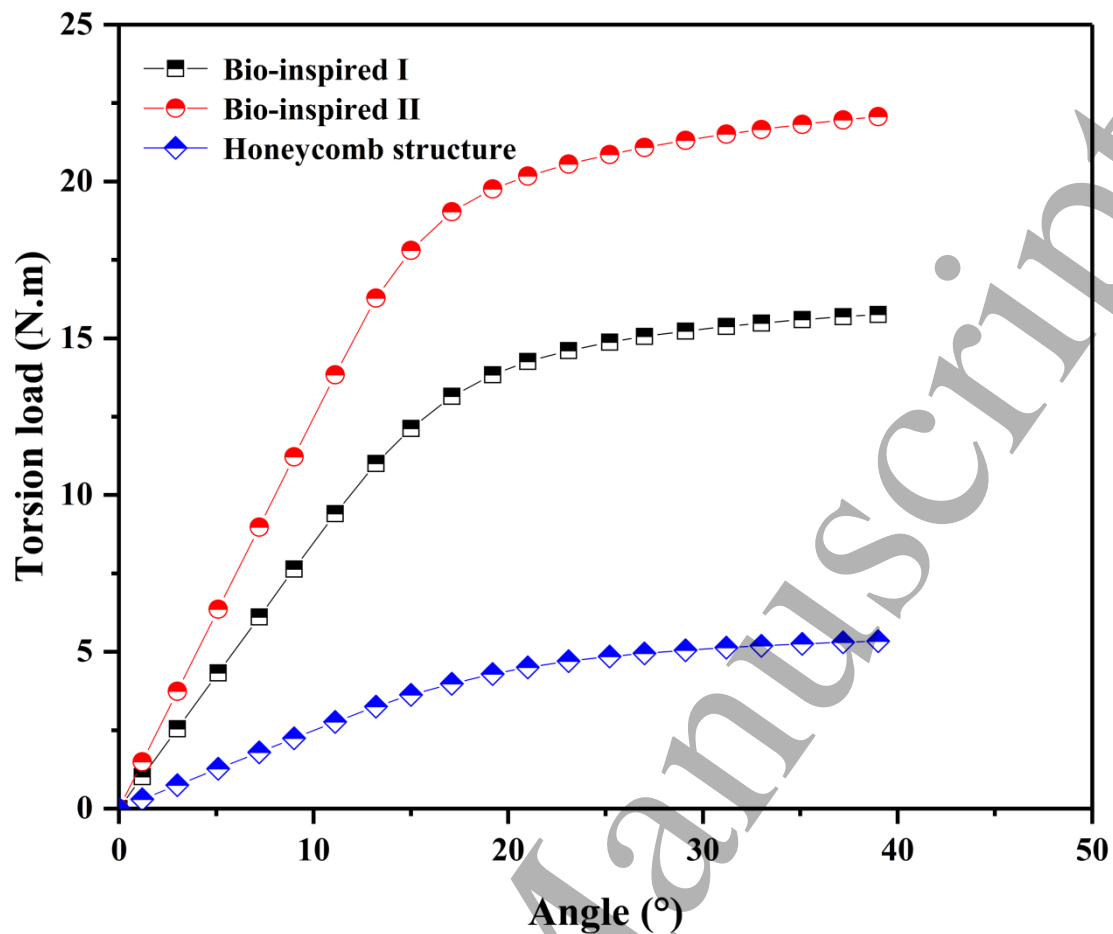


**Figure 8.** Torsion load displacement curve in FEA simulations of the three structures

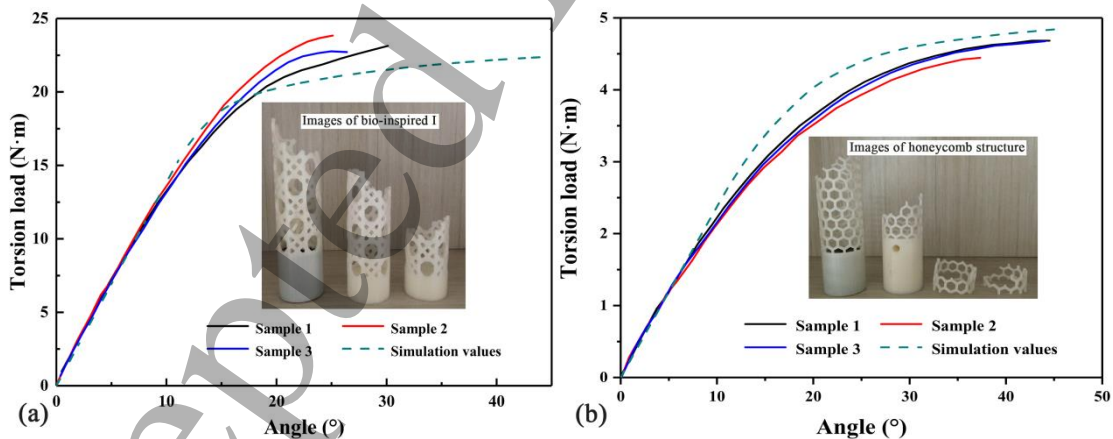


**Figure 9.** Torsion force-angle curves of bio-inspired structures, comparison was performed between FEM results and experimental results: (a) Bio-inspired I. (b) Honeycomb structure

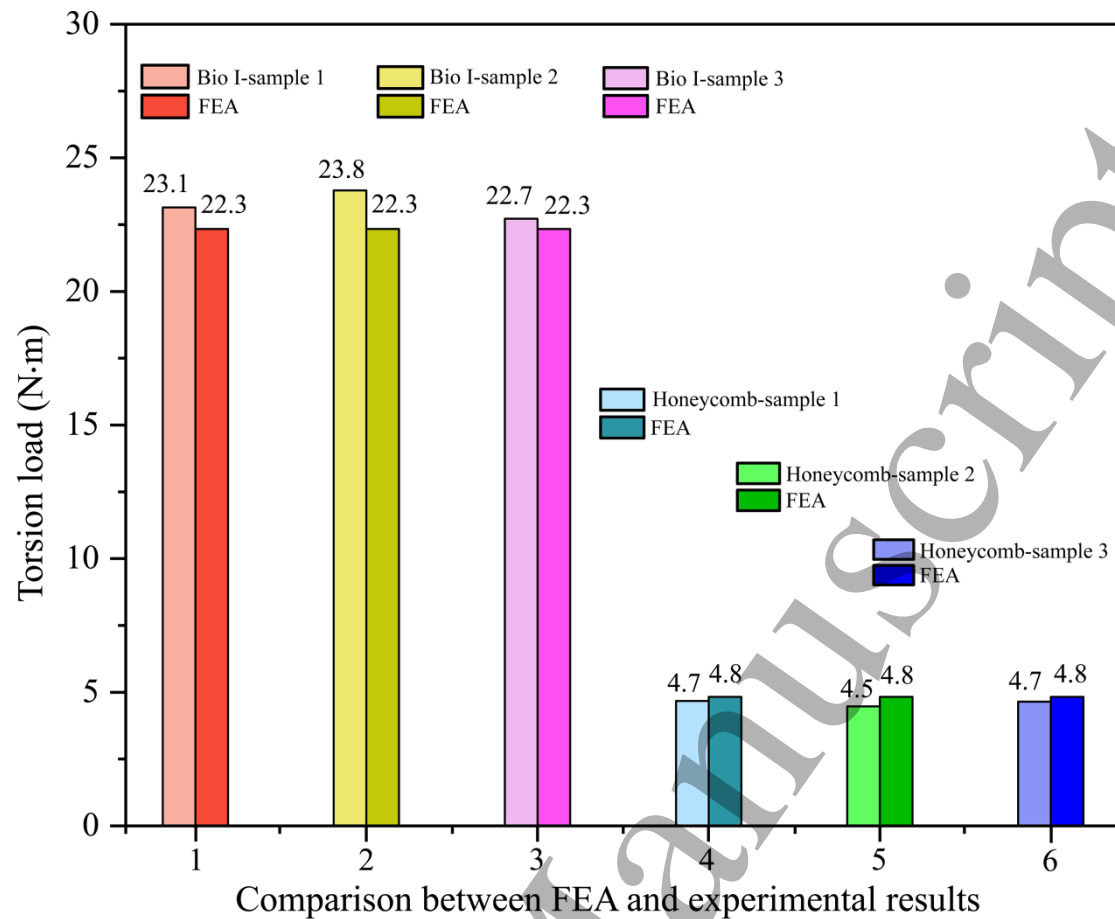


**Figure 10.** The differences of maximum torsion load between FEM and experimental results



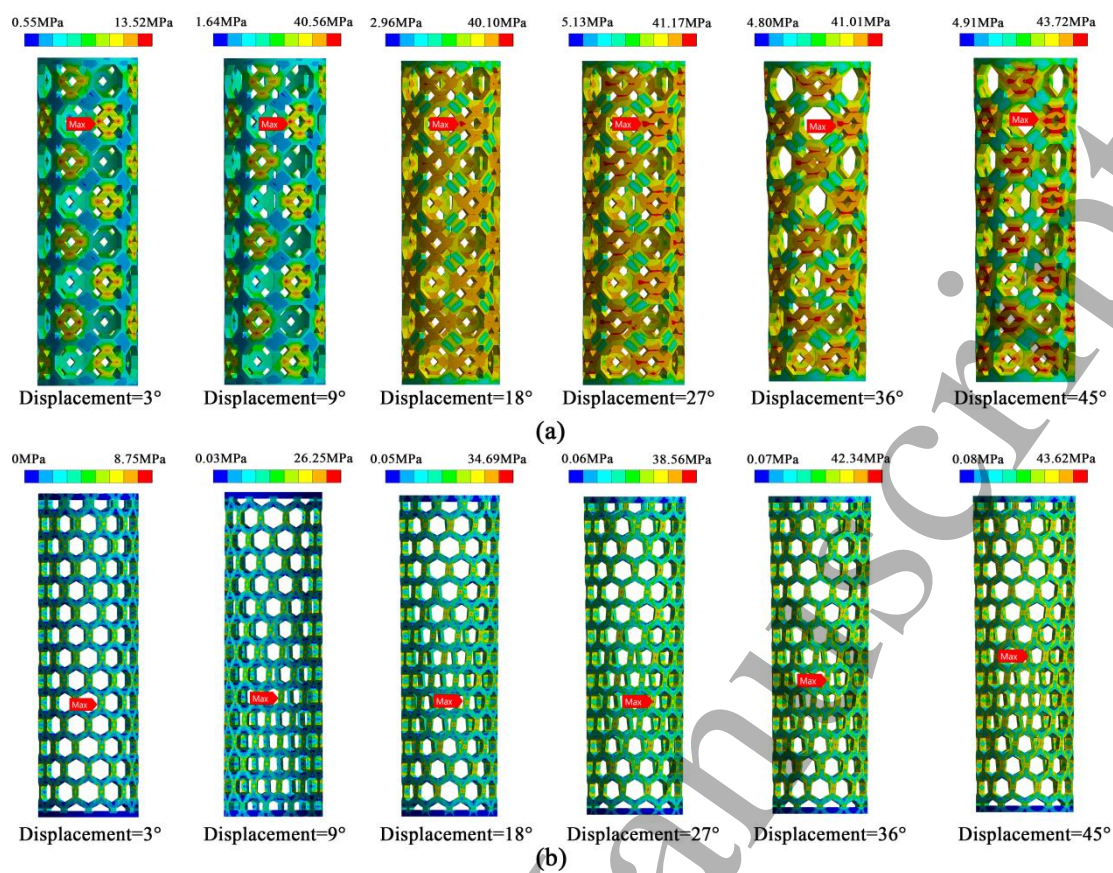


**Figure 11.** Diagrams of numerical deformation mode under torsion load: (a) bio-inspired I and (b) honeycomb structure

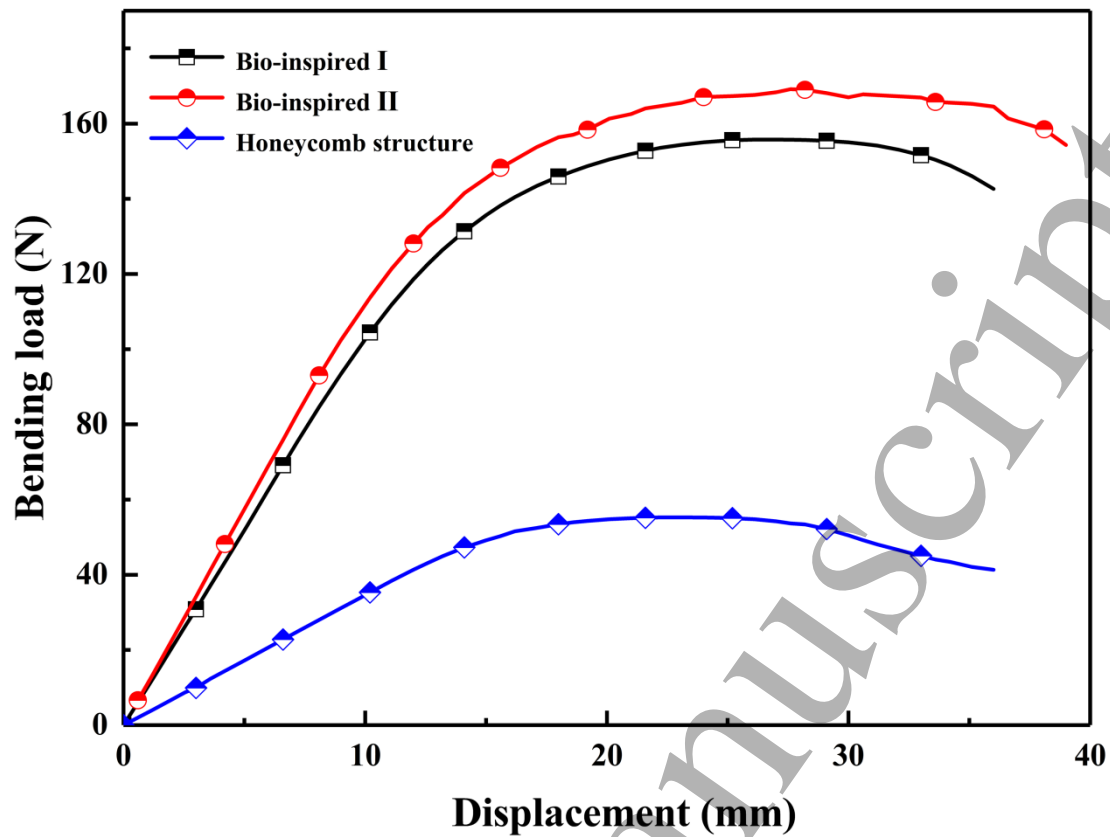


**Figure 12.** Bending load displacement curves in FEA simulations of the three structures

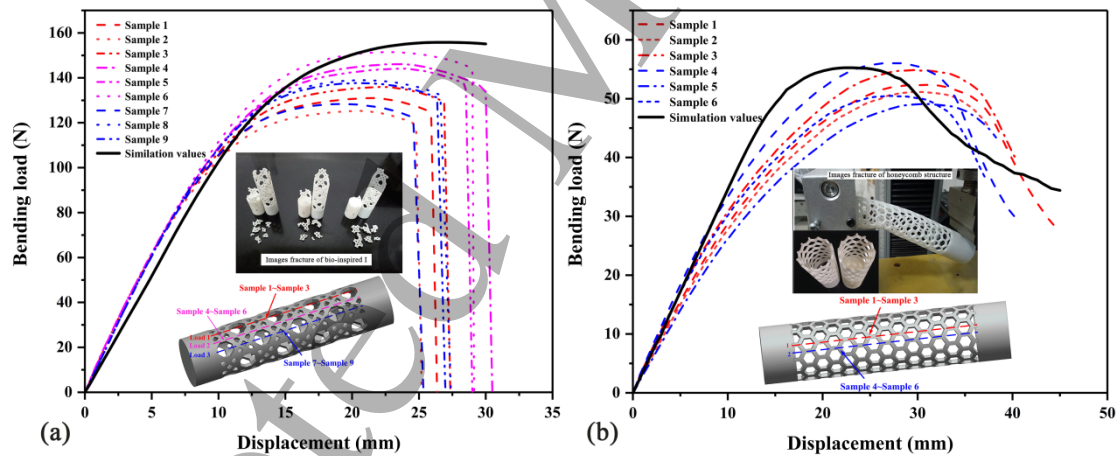


**Figure 13.** Comparison between FEM analysis and experimental results under the bending force for two structures: (a) Bio-inspired I. Load 1, load 2 and load 3 represent different load position on Bio-inspired I in the testing, respectively \*. The simulation results represent load condition 2. (b) Honeycomb structure. Load 1 and load 2 represent different load position on honeycomb structure, respectively. The simulation results represent load condition 1. Note\*: In our bending experiments,

1  
2  
3  
4  
5  
6  
7  
8  
9  
10  
11  
12  
13  
14  
15  
16  
17  
18  
19  
20  
21  
22  
23  
24  
25  
26  
27  
28  
29  
30  
31  
32  
33  
34  
35  
36  
37  
38  
39  
40  
41  
42  
43  
44  
45  
46  
47  
48  
49  
50  
51  
52  
53  
54  
55  
56  
57  
58  
59  
60

the force is loaded in the three difference positions at the solid end of the samples, the red dotted line, purple dotted line and blue dotted line are the lines which are through the three different force points respectively and paralleled to the axis of the tube, demonstrating the corresponding grid part of the tube

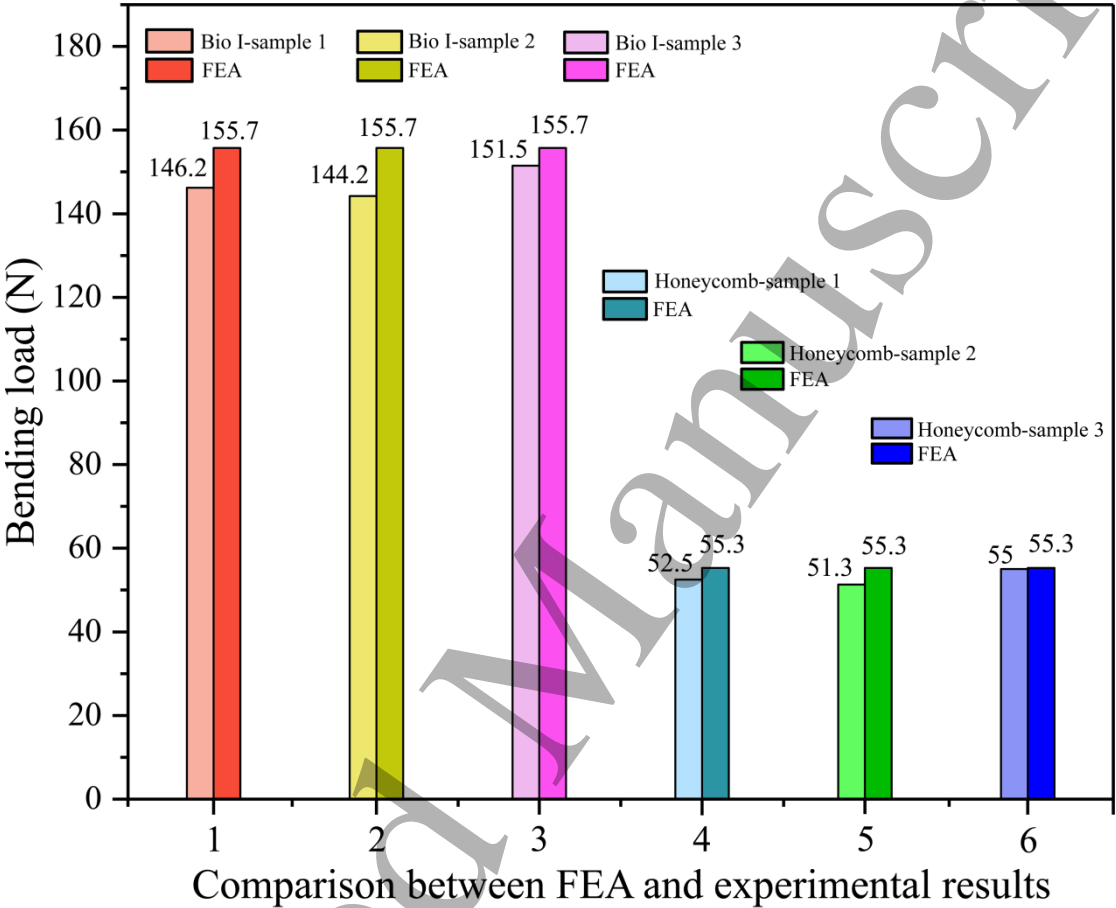


**Figure 14.** The differences of maximum bending load between FEM and experimental values



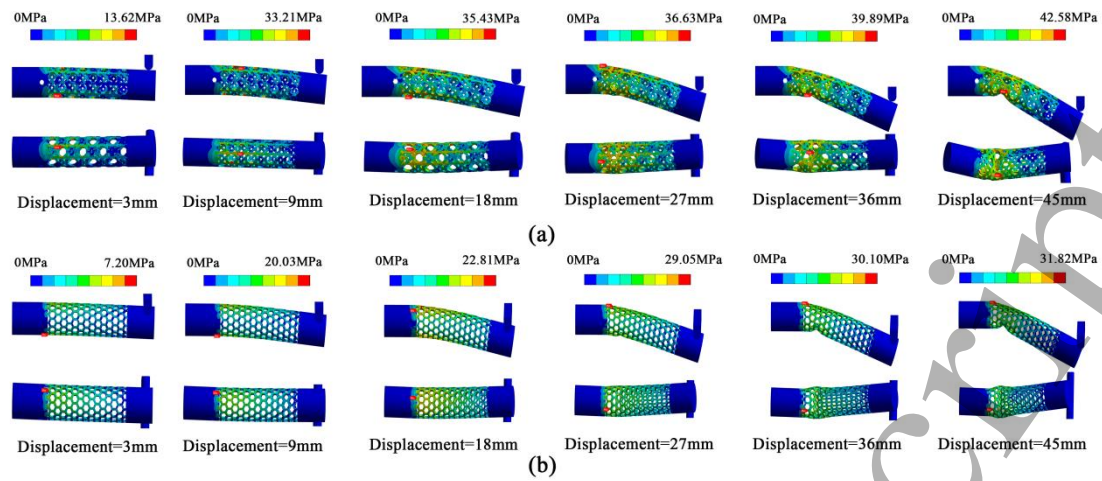


**Figure 15.** Diagrams of numerical deformation mode under bending load: (a) bio-inspired I and (b) honeycomb structure